Hydrogen and Corrosion Resistance of Nickel Superalloys for Gas Turbines, Engines Cooled Blades

Alexander I. Balitskii [1,2,*], Yuliia H. Kvasnytska [3], Lyubomir M. Ivaskevych [1], Kateryna H. Kvasnytska [3], Olexiy A. Balitskii [4], Inna A. Shalevska [3], Oleg Y. Shynskii [3], Jaroslaw M. Jaworski [5] and Jakub M. Dowejko [5,*]

[1] Department of Strength of the Materials and Structures in Hydrogen-Containing Environments, Karpenko Physico-Mechanical Institute, National Academy of Sciences of Ukraine, 79-601 Lviv, Ukraine

[2] Department of Mechanical Engineering and Mechatronics, West Pomeranian University of Technology in Szczecin, 70-310 Szczecin, Poland

[3] Department of Physico-Chemistry of Casting Processes, Physico-Technological Institute of Metals and Alloys NAS of Ukraine, 03-142 Kyiv, Ukraine

[4] Institute-Materials for Electronics and Energy Technology (i-MEET), Department of Materials Science and Engineering, Friedrich-Alexander-Universität Erlangen-Nürnberg, Energy Campus Nürnberg, Fürtherstraße 250, 90429 Nürnberg, Germany

[5] Research Center for Management of Energy Sector, Institute of Management, University of Szczecin, Cukrowa Street 8, 71-004 Szczecin, Poland

* Correspondence: balitski@ipm.lviv.ua (A.I.B.); jakub.dowejko@usz.edu.pl (J.M.D.)

Abstract: The paper presents the results of the analysis of the resistance to hydrogen and high-temperature salt corrosion of the developed alloy of the CM88Y type for the turbine blades of gas turbine engines for marine and power purposes in comparison with the industrial heat-resistant corrosion-resistant alloy CM88Y and the alloy for the protective coating of the SDP3-A blades. SDP3-A alloy was chosen as a reference sample, which has high hydrogen and corrosion resistance. The new heat-resistant alloy additionally contains such refractory metals as rhenium and tantalum, which are added to the composition of the alloy in order to increase operational characteristics while maintaining phase-structural stability. These are properties such as long-term and fatigue strength, characteristics of plasticity and strength at room and elevated temperatures. Therefore, the purpose of these studies was to determine the resistance to high-temperature salt corrosion of the developed alloy in comparison with the industrial heat-resistant nickel alloy and to evaluate the influence of alloying, hydrogen embrittlement of CM88Y and ZhS3DK alloys with different contents of chromium, boron, zirconium, hafnium, and yttrium were compared. The corrosion resistance of the materials was evaluated after crucible tests in a salt solution at a temperature of 900 °C for 30 h, according to the standard method. The corrosion resistances of alloys were determined by the mass loss, corrosion rate, and data from metallographic studies.

Keywords: heat-resistant alloy; high-temperature salt corrosion; gas turbine engine blade

1. Introduction

In the modern energy industry, almost 70 percent of all windings and rotor shafts of power generators with a capacity of more than 60 MW are cooled with hydrogen to prevent overheating under mechanical loads and friction [1–3]. The use of gaseous hydrogen as a heat carrier is based on its properties, namely, low density, a high specific heat capacity, and the highest thermal conductivity among all gases (0.168 W/(m·K). It is a 7–10 times better cooler than air [1–3]. Hydrogen gas under a pressure of 0.6 MPa circulates in a closed circuit to remove heat from the active parts and then is cooled by copper gas-water heat exchangers on the stator frame. Hydrogen has a very low viscosity, which helps to reduce the resistance losses in the rotor, which can be significant due to the high speed of rotation

of the rotor. The relevance of the problems of the explosiveness of hydrogen in a mixture with air oxygen and the hydrogen embrittlement of structural materials is increasing due to the development of hydrogen energy [4–8], which is caused by environmental threats associated with carbon dioxide emissions and their impact on climate change.

An important factor in the performance of an ecologically "green" hydrogen energy turbine (GET) and traditional turbine units (TA) (turbine + turbogenerator) is the degradation of structural materials under the influence of hydrogen contained in hydrogen-containing environments (HCE)—fuel and a cooling system. Hydrogen significantly worsens the operational characteristics of the engine combustion chamber, hot turbine track, turbine discs, and cooled blades [4,5,7–9]. Thus, it is relevant, on the one hand, in determining the influence of hydrogen on short-term strength and plasticity, low- and multi-cycle fatigue, static and cyclic crack resistance during the long-term service of structural materials, and on the other hand, the development of hydrogen-resistant steels and alloys and effective and safe hydrogen-containing mixtures for use as fuel and the thermal protection of parts of turbines and turbogenerators.

The trends in the development of cooling systems for high-temperature gas turbine engines and gas turbine installations (power, aviation, sea, and land transport) are based on modern technologies of the internal cooling of gas turbine blades (deformed, obtained by equal axis, direct crystallization's, single crystals technologies), external heat exchange, cyclone and vortex cooling, which imposes additional restrictions on construction materials. The external cooling of gas turbine blades, film cooling and technologies for obtaining profiled, anti-vortex holes in surface recesses, internal wall cooling, trends in temperature growth, and degree of compression require the creation of a new generation of alloyed high-temperature monocrystalline superalloys with an operating temperature of more than 1150 °C. Open and closed schemes of convective and convective-film cooling significantly affect the efficiency of gas turbines. Features of cooling nozzles and working blades are related to the diagram of heat exchange intensification. Modern methods of cooling different areas of the blade, improved schemes of the movement of the cooler in blades with internal cooling, and therefore new designs of blades include micro-finning of internal cooling channels (Figure 1) [8–10]. The distribution of the heat transfer coefficient along the contour of the blade, detection of the most stressed points on the inlet and outlet edges of the blade, the end surfaces of the nozzle apparatus are based on the concept of swirling flow and two-dimensional and three-dimensional schemes of cyclonic cooling. Vortex matrices for the internal cooling of gas turbine blades and their external and film cooling increase its efficiency and heat transfer coefficient. Calculations of film cooling (slot and discrete holes) and methods of increasing cooling efficiency by changing the geometry of the injection with the transition to the gap contribute to the creation of promising film cooling schemes.

The physical structure of the flow behind the profiled holes and anti-vortex holes, the geometrical parameters of the systems of paired holes, the use of additional anti-vortex holes, the supply of coolant in the trench, craters of different shapes and hemispherical recesses in the vanes with cooling inside the wall (Figure 1) are promising schemes, but have certain limitations that are superimposed with difficult-to-process modern superalloys made by single-crystal, directional crystallization, or powder metallurgy technologies.

An important problem of marine gas turbines is ensuring the resistance of materials against high-temperature salt corrosion. It is known that high-temperature salt corrosion leads to dangerous damage to the working blades of gas turbine engines (GTE). At the same time, damage to the hard-to-reach internal surfaces of the cooling channels significantly complicates the restoration of the blades. Working blades for new engines being developed must withstand a temperature of 950 °C, compared to the blades currently working (working temperature 900 °C). Blades for turbines of various purposes are made of heat-resistant nickel-based alloys. To reduce the high-temperature corrosion of blades, 3 to 20% chromium is added to these alloys. Therefore, when improving the chemical composition of heat-resistant alloys for the blades of gas turbines for marine and energy purposes, it is necessary to conduct research on corrosion resistance [11,12].
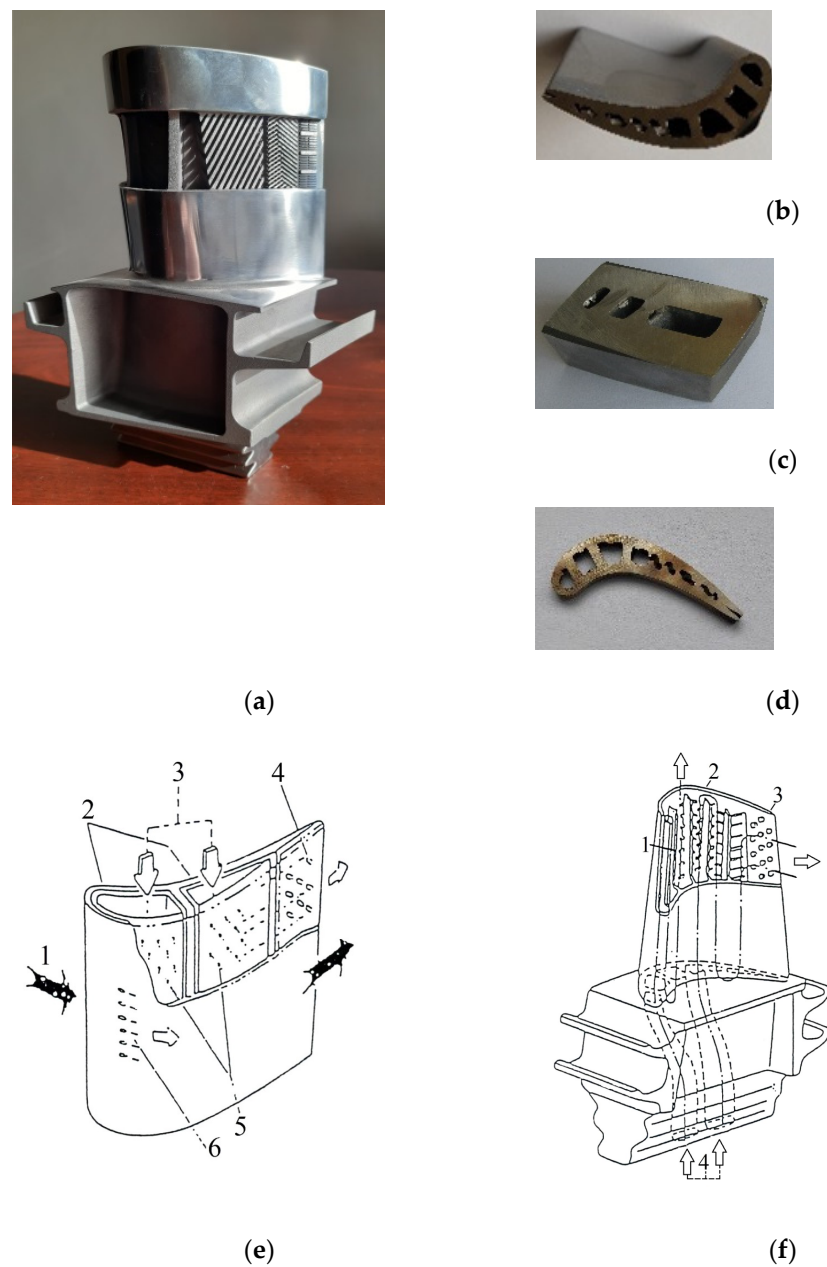
Figure 1. Blade of a DN80 power gas-turbine engine (**a**), cross-sections of its parts (**b–d**) and structure of the advanced cooling turbine blade: stationary blade (1—combustion gas, 2—core plug, 3—cooling air, 4—pin fin, 5—impingement cooling, 6—film cooling hole) (**e**); moving blade (1—turbulence promoter, 2—serpentine cooling channel, 3—pit fin, 4—cooling air) (**f**).

The formation of an updated phase composition of alloys by alloying with a complex of refractory elements, which would combine a high resistance to high-temperature corrosion with heat resistance, is an important urgent fundamental material science problem. The additional introduction of refractory elements, such as rhenium, tantalum, ruthenium, etc. with a balanced chromium content, will provide an increase in heat resistance without the deterioration of corrosion resistance [13–22].

In gas turbine engines, high-temperature corrosion manifests itself mainly due to the increased content of sulphur in diesel and turbine fuel and additionally the ingress of seawater salts in ship engines. The presence of sodium and sulphur in diesel fuel leads to the formation of a certain amount of liquid sodium sulphated particles in the hot part of the turbine in a dusty state. The salt accumulated in the compressor is separated from

the blades in the form of fractions of different sizes and enters the hot part of the turbine, mostly on the engine blades. Salt mixtures on the blades, depending on the operating temperature of the gas turbine engine during operation, can be both in a solid and liquid state [20–25].

When sodium sulphate is deposited on the surface of the alloy and interacts with the latter, sodium oxide and reducing metal are formed, as well as sulphur, which forms one or another type of sulphide with the components of the alloy. In particular, nickel sulphide can form eutectics of the M-MS type with a melting point of 645 °C. The latter reacts with oxygen penetrating through the molten salt, with the formation of metal oxide (MO), metal sulphides, and selenides (MS). The metal sulphide dissolves the metal again with the formation of the M-MS eutectic.

This process is enhanced by the fact that molten salt easily penetrates to the surface of the metal through pores and microcracks in the scale. Atomic oxygen leads to the rapid impoverishment of the surface layers of the metal with alloying elements (to obtain almost pure nickel) and intensively moves deep into the metal. At the same time, elements with a high affinity for oxygen are oxidized, and islands of unoxidized nickel join the scale mass, being oxidized to NiO. Taking into account the above analysis of the scale composition that forms on the turbine blades during operation and is the cause of high-temperature salt corrosion, the purpose of the work is the evaluation of the performance of a new heat-resistant alloy in comparison with other known and standardized alloys used for a similar application and to carry out a study of the corrosion and hydrogen resistance of heat-resistant nickel alloys for the working blades of gas turbine engines.

2. Materials and Methods

The research was conducted on samples of a new heat-resistant alloy [23–47], a heat-resistant nickel alloy that is widely used in the production of CM88Y (Ni60Cr16Co11Mo2Ti4Al4W6NbHfYBZr) [10] and the SDP3-A (Cr32Ni8) alloys. The developed heat-resistant alloy (Ni base; 0.04–0.07 C; 12.3–13.2 Cr; 3.0–3.5 Al; 1.8–2.3 Ti; 6.8–7.5 Co; 0.03–0.05 Zr; 0.45–0.50 Fe; 0.9–1.4 Mo; 6.0–6.6 W; 0.1–0.5 Nb; 2.5–4.3 Ta; 3.7–4.3 Re by weight), which is additionally alloyed with rhenium and tantalum, was created in order to increase operational properties (long-term strength, fatigue strength, plasticity characteristics, and strength at room and elevated temperatures) while maintaining phase-structural stability and corrosion resistance [25,26]. The SDP-3A alloy is mainly used as a protective coating for high-pressure turbine blades of modern marine and gas pumping gas turbine engines [26]. The choice of such alloys is due to the purpose of comparing the received evaluation criteria regarding the stability of the new heat-resistant alloy. Castings with an oriented dendritic structure were obtained by vacuum remelting in a ceramic mold with a diameter of 200 mm and a height of 400 mm by the method of directional crystallization in a foundry unit VIM-25-175C (manufactured by SECO-WARWICK, Poland) [21,25]. To obtain cylindrical samples of each alloy, a standard block (a corundum (Al_2O_3) mold was used to obtain eight samples weighing 7.2 kg. The temperature of pouring the melt was 1560–1580 °C. The temperature was controlled by a thermocouple and an optical two-color pyrometer (Mikron type device, model M-780). Samples of the SDP-3A alloy were cut from castings that were melted by electron beam melting at the production of special alloys for protective coatings. The chemical composition of superalloys is developed in such a way that the oxides of chromium, aluminum, and tantalum on the surface of the blades protect them from high-temperature corrosion [12,15–113], so it is advisable to study the corrosion resistance on samples with oxides. Hydrogen embrittlement was studied on polished samples.

The microstructure of the surface layer of samples from the experimental alloy is similar to the structure of the CM88Y alloy. In addition to the depth of surface corrosion, the amount of penetration of defects into the alloy along the interphase grain boundaries was assessed, which was studied using a Neofot-3M optical microscope. Grain sizes and the depth of corrosion defects were determined with the help of an optical microscope

Neofot-3M with an accuracy of ±1 μm. Average values of grain sizes were obtained by the random secant method [112,113]. Additionally, a visual method was used to estimate the macrograin size in the polycrystalline sample according to the instructions of gas turbine engine manufacturers. The method consists in comparing the macrostructure of the test samples with reference scales, which are a set of standard macrophotographs, each of which shows grains of a certain size at the same magnification. At the same time, the grain size is characterized by a reference structure that corresponds to certain cross-sectional dimensions of the grain.

To study the corrosion properties, cylindrical samples with a diameter of 8 mm and length of 15 mm were cast, which were subjected to mechanical and thermal treatment according to the standard regime: 1170 ± 10 °C, 4 h, cooling in air; 1050 ± 10 °C, 4 h, cooling in air; and 850 ± 10 °C, 16 h, cooling in air. The dimensions of the samples were determined using a micrometer MK 50–1 with an accuracy of ±5 μm (Figures 1a and 2a). The studied materials were degreased by washing three times in ethyl alcohol or acetone. After that, they were air-dried for 20 min. Then, they were weighed on analytical scales VLR-200 with an accuracy of $\pm 1 \times 10^{-4}$ g. Metal samples were placed in dried corundum crucibles and filled to the top with a mixture of 25% NaCl + 75% Na_2SO_4 salts. The amount of this mixture (Q) was calculated according to the known formula [21,26]:

$$Q = h \cdot r (S_T - S_o), \tag{1}$$

where h—salt melt height; r—salt density (for this mixture r = 2.5 g/cm^3); S_T—the area of the internal section of the bottom of the crucible; and So—total surface area of the sample, m^2.

(**a**)   (**b**)

(**c**)
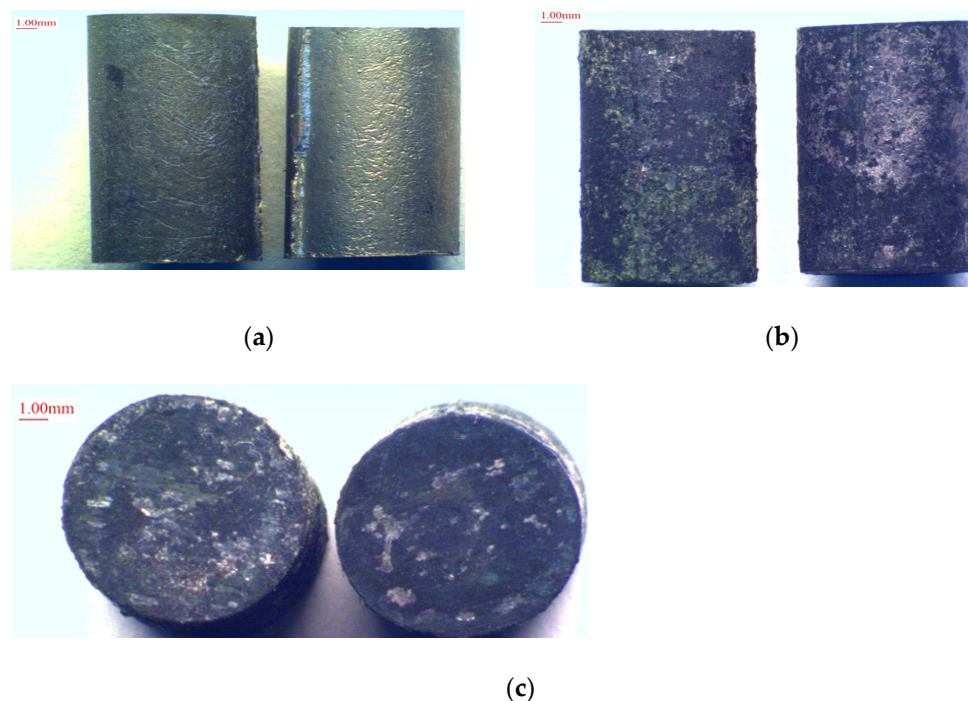
Figure 2. The appearance of samples before (**a**) and after corrosion tests (**b**,**c**) from the CM88Y alloy (left) and the experimental alloy (right).

The crucibles with samples were placed in a metal container with a lid, which is made of a heat-resistant alloy of the XH60BT type (EI 868). The tests were carried out at a temperature of 900 °C in molten salts for 30 h in a resistance furnace of the SNOL-2,5.1,6.1/9 type. After that, the samples were extracted from the molten salt with tweezers and washed under running water for 15 min. The samples cleaned in this way were then boiled for one hour in heat-resistant glasses to separate scale and salt from their surface. It

was washed again under running water for 10 min and dried at a temperature of 120 °C for 10 min. The final removal of scale from the surface of the samples was carried out in a melt of the following composition: 70% NaOH, 25% NaNO$_3$, and 5% NaCl at a temperature of 450 °C for 1.5 h. After that, the samples were removed from the crucibles, cooled, and thoroughly washed with a solution of soda ash (Na$_2$CO$_3$) for 15 min. The final removal of the oxide film from the surface of the sample was carried out in a solution with the following composition: 20% H$_2$SO$_4$, 1.5% HNO$_3$, and 2.5% NaCl, and the rest distilled H$_2$O at room temperature for 3–5 min. After that, the samples were dried, finally degreased, and weighed [26].

The resistance of alloys to high-temperature salt corrosion was determined on the basis of mass loss and data from metallographic studies (the depth of the spread of corrosion in the metal). After removing the corrosion products, the mass of the samples was determined on analytical scales with an accuracy of 0.0001 g. The amount of specific mass loss was calculated according to the formula

$$q = (m_0 - m)/S \tag{2}$$

where m_0—mass of the sample before the corrosion test, m—mass of the same sample after the removal of corrosion products, and S—initial surface area of the sample.

A well-known formula was used to calculate the corrosion rate:

$$Vq = \Delta m/S\tau, \tag{3}$$

where Vq—average corrosion rate; $\Delta m = m_0 - m_\text{к}$; m_0—the initial mass of the sample; $m_\text{к}$—the mass of the sample after the tests; S—the total frontal area of corrosion damage; and τ—exposure time.

The depth of corrosion damage on the surface d and the internal corrosion h of the samples were studied using a Neofot-3M optical microscope. The depth of external corrosion was determined by the half difference of the initial and final diameters of the sample:

$$d = (d_0 - d_\text{к})/2, \tag{4}$$

where d—the depth of external corrosion; d_0—the initial diameter of the sample, m; and $d_\text{к}$—the diameter of the sample after testing, m. This procedure dissolves only the corrosion products that formed on the surface of the samples and as a result of the penetration of defects into the alloy along the grain boundaries [20–22,29].

Short-term stretching (static tensile tests) was carried out at a speed of 0.1 mm/min (by displacement rate $V_\text{d} = 6.7 \times 10^{-5} \text{ s}^{-1}$) in the air and gaseous hydrogen under the pressure 0 . . . 30 MPa on standard cylindrical specimens with a working part diameter of 5 mm. This type of sample was used to determine the high-cycle durability submitted to cyclic loading on the scheme "pure bending with rotation" at a fixed strain amplitude with a 50 Hz frequency at temperature 800 °C.

3. Results

3.1. High-Temperature Salt Corrosion of Alloys

The resistance of alloys to high-temperature salt corrosion was determined by mass loss and according to data from metallographic studies (the depth of the spread of corrosion in the metal). The results of studies of corrosion resistance of the samples are presented in the table. The appearance of the samples after corrosion tests is shown in Figures 2 and 3, and their structure is shown in Figure 4. The macrostructure of all alloy samples has a polycrystalline structure with an average grain size of 0.5–4.0 mm. (Table 1). A statistical analysis of experimental data was carried out based on the values of at least five obtained results. Average values of determined quantities and root mean square deviations were calculated. The testing of the null statistical hypothesis showed that all experimental results meet the Pearson consistency criterion [114] with a significance level of $\alpha = 0.05$.
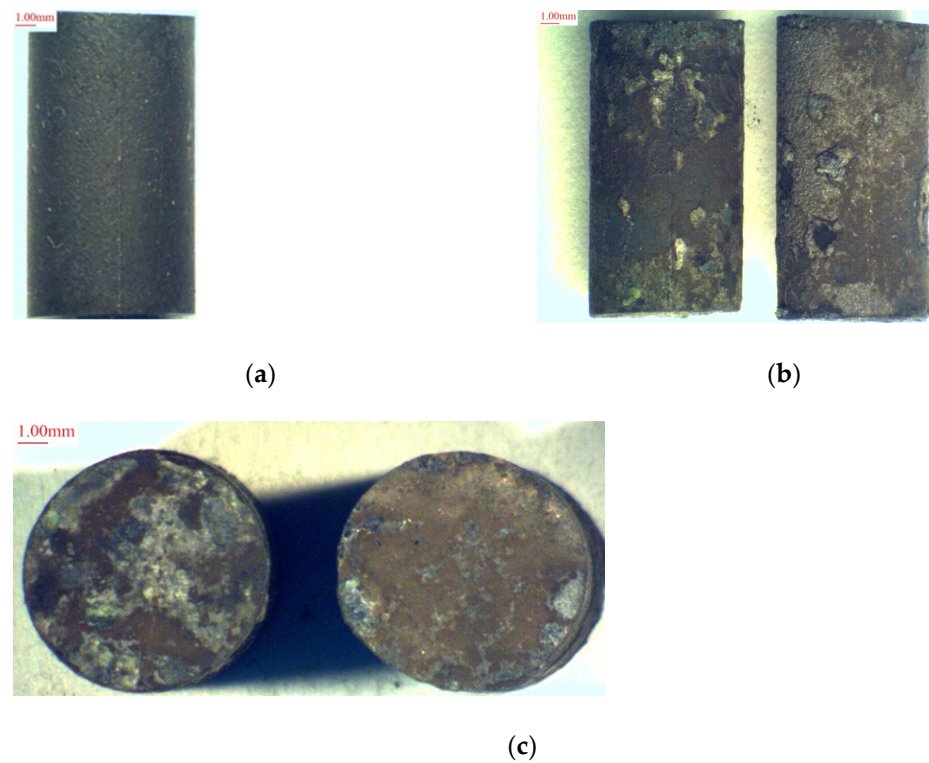
(**a**)

(**b**)

(**c**)

Figure 3. The appearance of samples before (**a**) and after corrosion tests ((**b**,**c**)—sample No. 5, 6 according to the table) from the SDP3-A alloy.
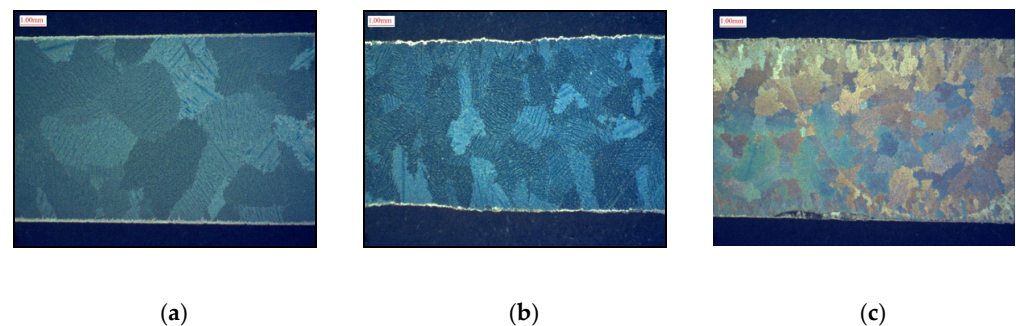

(**a**)

(**b**)

(**c**)

Figure 4. Macrostructure after tests (longitudinal section) of samples from the CM88Y alloy (**a**); experimental alloy (**b**); SDP3-A (**c**).

Table 1. Results of high-temperature salt corrosion tests.

| Alloy | Experimental | | CM88Y | | SDP 3-A | |
Sample Number	1	2	3	4	5	6
Grain size in the alloy, $\times 10^{-3}$ m	1.0–2.0	1.5–3.0	1.0–3.0	3.0–4.0	0.5–1.0	0.5–1.0
Specific mass loss, after 30 h, kg/m^2	0.287	0.278	0.353	0.289	0.053	0.121
Corrosion rate, Vq, kg/m^2 h	0.0089	0.0096	0.0118	0.0096	0.0018	0.004
Depth of external corrosion, $d \times 10^{-3}$ m	0.28	0.05	0.05	0.24	0.30	0.27
Depth of internal corrosion, $h \times 10^{-3}$ m	0.05–0.10	0.05–0.10	0.12–0.15	0.10–0.12	0.20–0.40	0.05–0.30

The determined indicators of corrosion resistance, namely the rate of corrosion and the specific mass loss of the new heat-resistant alloy, are at the level of the indicators of the industrial alloy CM88Y and meet the requirements of the standard [24–29]. It was established that the same corrosion damage of intergraine boundaries is observed in the samples from the CM88Y alloy and the experimental alloy. The depth of internal damage, on average, is 0.05–0.28 mm. When examining the scale of experimental samples of the

developed alloy, the presence of refractory oxide Ta_2O_3 is observed along with protective oxides NiO and Cr_2O_3. The test results showed that, with increased strength characteristics, the developed alloy has resistance to high-temperature salt corrosion at the level of standard heat-resistant nickel alloy CM88Y and meets the requirements of regulatory documents. Alloying the melt with tantalum in the amount (2.5–4.3% by weight) allows for reducing the chromium content in castings from 15.5–16.0 to 12.3–13.2% by weight and makes it possible to obtain vanes with high corrosion resistance in high-temperature salt environments from the experimental alloy. The depth of corrosion defects was studied using a Neofot-3M optical microscope. The structure of the surface layer of samples from the experimental alloy is similar to the structure of the CM88Y alloy. In addition to the depth of surface corrosion, the amount of penetration of defects into the alloy along the grain boundaries was evaluated. It was established that the same corrosion damage of intergraine boundaries is observed in the samples from the CM88Y alloy and the experimental alloy. The depth of internal damage, on average, is 0.05–0.28 mm. The smallest depth of corrosion damage is observed in samples of SDP3-A alloy.

On the basis of previous studies of this experimental alloy, in particular, a micro-X-ray spectral analysis of blades and literary sources, Ta_2O_3 oxide is formed during tests in molten salts [20–23]. Ta_2O_5 can be formed with free access to oxygen.

It can be seen from the table that CM88Y and experimental alloys are characterized by a high resistance to salt corrosion. This is due to the fact that a dense oxide film forms on the surface of samples from such alloys, which prevents the deep penetration of chemicals into the volume of the material. The addition of tantalum leads to the formation of carbides of the MeC type, and therefore chromium is not consumed for the formation of $Cr_{23}C_6$, but remains in the matrix. As a result, protective oxide Cr_2O_3 is formed, which increases the corrosion resistance of the material. When examining the scale of experimental samples of the developed alloy, the presence of the refractory oxide Ta_2O_3 is observed along with protective oxides NiO and Cr_2O_3. It is likely that Ta_2O_3 oxide, unlike Mo, W, and Nb oxides, which react with Na_2SO_4 and contribute to the dissolution of NiO, does not interact with sodium sulphate and thereby contributes to the formation of a protective film.

3.2. The Influence of Hydrogen on the Properties of Alloys for Gas Turbine Blades

The degree of hydrogen embrittlement (HE) of the CM88Y (Ni60Cr16Co11Mo2Ti4Al4W6NbHfYBZr) alloy and the heat-resistant casting alloy ZhS3DK (Ni74Cr12Co10Mo4Ti3Al4W3BCe), which is used for casting blades of aviation gas turbine engines [32], were compared. The chemical composition of the materials is given in Table 2. ZhS3DK alloy contains less chromium, which impairs its corrosion resistance, as well as titanium and tungsten, which reduces its strength in the whole investigated temperature range (Figure 5). The high corrosion and heat resistance of the CM88Y alloy is provided by the presence in its composition of boron, zirconium, hafnium, and yttrium [11–22,33,34], which are absent in the alloy ZhS3DK (Table 2). Rhenium significantly increases the melting temperature of nickel alloys and has a noticeable effect on the thermal stability of the γ-matrix and γ'-phase. It is included mainly in the γ-solid solution (its content in the γ'-phase is small, about 0.2%), thereby contributing to the displacement of such effectively stabilizing elements as aluminum and tantalum from the solid solution into the γ'-phase. Rhenium slows down the diffusion processes occurring at high temperatures in heat-resistant nickel alloys. Therefore, it is introduced into such materials to increase heat resistance and creep [115]. Thus, the introduction of rhenium and tantalum into the new heat-resistant, corrosion-resistant alloy contributed to an increase in the solidus and liquidus temperatures from 1270–1330 (CM88Y alloy) to 1320–1370 °C, respectively, as well as the dissolution temperature of the strengthening γ'-phase $Ni_3(Al, Ti)$. This made it possible to increase the operating temperature of blades made of the new alloy compared to the CM88Y alloy by ~50 °C [21]. The effect of Re on the corrosion and hydrogen resistance has not been studied enough. There are no systematic data on the effect of Re on the corrosion and hydrogen resistance in the literature.

Table 2. Chemical composition of the investigated nickel superalloys.

Alloy	Content of Elements, wt.% (Ni-Balance)												
	C	Cr	Co	Mo	Ti	Al	W	Nb	Hf	Y	B	Zr	Ce
CM88Y	0.07	15.6	11.0	2.0	4.20	3.8	5.90	0.2	0.3	0.3	0.07	0.05	–
ZhS3DK	0.07	12.0	10.3	4.2	2.99	4.4	2.96	–	–	–	0.01	–	0.01
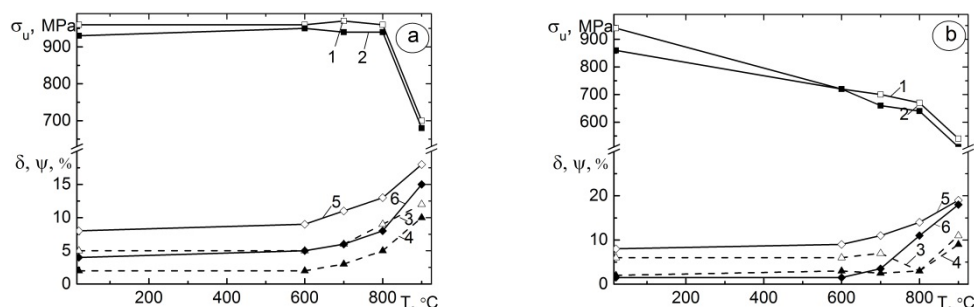
Figure 5. Temperature dependences of the ultimate strength σ_u (1, 2), relative elongation δ (3, 4) and reduce of area ψ (5, 6) of CM-88Y (**a**) and ZhS3DK (**b**) alloys in air (1, 3, 5) and water at a pressure of 30 MPa (2, 4, 6).

The strength of the heat-resistant alloy CM88Y changes little in the temperature range of 20–800 °C, sharply decreases when the temperature rises to 900 °C, and almost does not change under the influence of hydrogen (Figure 5a). The ultimate strength σ_u of the ZhS3DK alloy with a lower content of refractory and intermetallic-forming elements is significantly lower (Table 2, Figure 5b).

Dispersion-hardening nickel alloys with intermetallic strengthening are strongly embrittled by gaseous hydrogen, which is manifested in the deterioration of plasticity characteristics during short-term static stretching [35–41]. This is especially characteristic of cast materials with a non-homogeneous structure, liquation, and coarse grains [29,36,47–115]. It is known that the sensitivity to hydrogen and the number of areas of intergranular fracture in heat-resistant nickel alloy samples decrease with decreasing grain size, even though the hydrogen concentration in coarse-grained samples is lower than in fine-grained ones [35,37–75]. As in the case of deformable alloys [38–42], the degree of hydrogen embrittlement of cast alloys depends on their chemical composition and heat treatment regimes, which determine the features of the material structure [29,36].

The plasticity characteristics of both alloys are greatly reduced in hydrogen at a pressure of 30 MPa (Figures 5 and 6). Thus, at room temperature, the relative elongation of samples from the CM88Y alloy decreases by 2.5 times, the reduction of area—by 2 times, from the ZhS3DK alloy—by 3 and more than 5 times, respectively (Figure 5a,b). In accordance with the ASTM standard G129-2000(R2013), the sensitivity of materials to hydrogen embrittlement was compared by the coefficient of influence of hydrogen on the reduction of area of the samples β_ψ (Figure 6). The CM88Y alloy with higher strength is significantly embrittled at 800 °C and is sensitive to the action of hydrogen even at 900 °C (Figures 5 and 6). It has been established that increasing the hydrogen durability (HD) of austenitic iron-nickel steels and alloys is achieved by forming a structure with thin grain boundaries with increased cohesive energy by introducing boron, lanthanum, and zirconium, by optimizing the morphology of intermetallic [35,39–42,44–115]. Therefore, the ZhS3DK alloy, in which there are none of these alloying elements, is much more embrittled by hydrogen in the temperature range of 20–700 °C. At higher temperatures, its strength decreases sharply, and the effect of hydrogen weakens (Figure 6).

High-cycle fatigue (HCF) is an important characteristic of the performance of rotating parts of power equipment, such as rotors, discs and blades of turbines and engines [46–50]. The endurance limit of alloys was determined in a hydrogen chamber for the high-cycle fatigue (HCF) materials [48] in air and hydrogen at a pressure of 30 MPa at a temperature of

800 °C. At this temperature, the CM88Y alloy retains high strength and sensitivity to hydrogen embrittlement, both under static tensile tests (Figure 6) and under fatigue loads (Figure 7, curves 1, 2). For all load amplitudes, the fatigue limit (FL) of the ZhS3DK alloy is significantly lower and changes little under the influence of hydrogen (Figure 7, curves 3, 4).
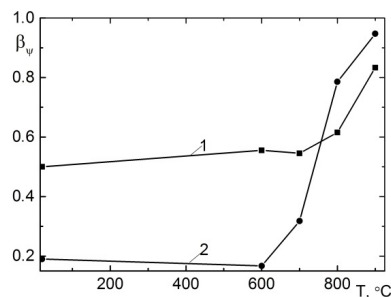

Figure 6. Temperature dependence of the coefficient of influence of hydrogen at a pressure of 30 MPa on the reduction of area β_ψ of samples from alloys CM-88Y (1) and ZhS3DK (2).
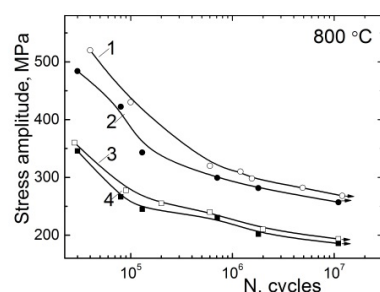

Figure 7. Endurance curves of the CM88Y (1, 2) and ZhS3DK (3, 4) in air (1, 3) and hydrogen at a pressure of 30 MPa (2, 4).

4. Conclusions

The carried out studies indicate that the resistance to high-temperature salt corrosion of the experimental nickel alloy is close in value to the values characteristic of the standard heat-resistant alloy CM88Y and meets the requirements of the regulatory documentation. Alloying the developed heat-resistant alloy with tantalum in the amount (2.5–4.3% by weight) allows for reducing the chromium content in castings from 15.5–16.0 to 12.3–13.2% by weight and obtaining blades with high corrosion resistance in high-temperature salt environments.

During static tensile tests, hydrogen at a pressure of 30 MPa has a negligible effect on the strength and significantly reduces the plasticity characteristics of cast heat-resistant nickel alloys CM88Y and ZhS3DK alloy, in which there are no boron, lanthanum, and zirconium, which are much more embrittled by hydrogen in the temperature range of 20–700 °C. At temperature 800 °C the CM88Y alloy retains high strength and sensitivity to hydrogen embrittlement both under static tensile tests and under fatigue loads. For all load amplitudes, the fatigue endurance of the ZhS3DK alloy is significantly lower and changes little under the influence of hydrogen.

Data Availability Statement: Not applicable.

Conflicts of Interest: Authors declare any personal circumstances or interest that may be perceived as inappropriately influencing the representation or interpretation of reported research results.Nomenclature and Abbreviations

Nomenclature and Abbreviations

σ_u	ultimate tensile strength (UTS)
$\sigma_{0,2}$	yield strength (YS)
σ_{-1}	fatigue limit (FL)
N	number of cycles
δ	elongation
ψ	reduction of area
C_H	hydrogen concentration
wppm	weight parts per millions
GTE	gas turbine engine
GET	environmentally 'greener' hydrogen energetic turbine
HCF	high-cycle fatigue
LCF	low-cycle fatigue
RPM	rotation per minute
HD	hydrogen durability
HCE	hydrogen-containing environment
HE	hydrogen embrittlement
MO	metal oxide
MS	metal sulphides and selenides
TA	turboaggregate (turbine + turbogenerator)

References

1. Nagano, S.; Kitajima, T.; Yoshida, K.; Kazao, Y.; Kabata, Y.; Murata, D.; Nagakura, K. Development of world's largest hydrogen-cooled turbine generator. *IEEE Power Eng. Soc. Summer Meet.* **2002**, *2*, 657–663. [CrossRef]
2. Kumar, R.; Kumar, A. Assessment of impact of hydrogen cooled generator on power system loadability enhancement. In Proceedings of the 2015 International Conference on Energy, Power and Environment: Towards Sustainable Growth (ICEPE), Shillong, India, 12–13 June 2015; pp. 1–6. [CrossRef]
3. Dhivya, S. 210 MW turbo generator's hydrogen gas cooling system online monitoring and controlling using node red flow based IOT. *Malaya J. Mat.* **2020**, *S*, 3225–3231. [CrossRef]
4. Griebel, P. Gas Turbines and Hydrogen. In *Hydrogen Science and Engineering: Materials, Processes, Systems and Technology*; Wiley: Hoboken, NJ, USA, 2016; Volume 2, pp. 1011–1032. [CrossRef]
5. Stefan, E.; Talic, B.; Larring, Y.; Gruber, A.; Peters, T.A. Materials challenges in hydrogen-fuelled gas turbines. *Int. Mater. Rev.* **2022**, *67*, 461–486. [CrossRef]
6. Bothien, M.R.; Ciani, A.; Wood, J.P.; Fruechtel, T.G. Decarbonized power generation with gas turbines by using sequential combustion for burning hydrogen. *J. Eng. Gas Turbines Power* **2019**, *141*, 121013. [CrossRef]
7. Chiesa, P.; Lozza, G.; Mazzocchi, L. Using hydrogen as gas turbine fuel. *J. Eng. Gas Turbines Power* **2005**, *127*, 73–80. [CrossRef]
8. Lambert, H.; Roche, R.; Jemeï, S.; Ortega, P.; Hissel, D. Combined cooling and power management strategy for a standalone house using hydrogen and solar energy. *Hydrogen* **2021**, *2*, 207–224. [CrossRef]
9. Balitskii, A.; Krohmalny, O.; Ripey, I. Hydrogen cooling of turbogenerators and the problem of rotor retaining ring materials degradation. *Int. J. Hydrog. Energy* **2000**, *25*, 167–171. [CrossRef]
10. Unnikrishnan, U.; Yang, V. A review of cooling technologies for high temperature rotating components in gas turbine. *Propuls. Power Res.* **2022**, *11*, 293–310. [CrossRef]
11. *Technical Database for Hydrogen Compatibility of Materials*; Sandia National Laboratories: California, CA, USA, 2022; Available online: https://h2tools.org/technical-database-hydrogencompatibility-materials (accessed on 27 November 2022).
12. Wee, S.; Do, J.; Kim, K.; Lee, C.; Seok, C.; Choi, B.-G.; Kim, W. Review on mechanical thermal properties of superalloys and thermal barrier coating used in gas turbines. *Appl. Sci.* **2020**, *10*, 5476. [CrossRef]

13. Glotka, A. Prediction thermo-physical characteristics heat-resistant nickel alloys directional crystallization. *Acta Metall. Slovaca* **2021**, *27*, 68–71. [CrossRef]

14. Sheykhlari, F.A.; Moghanaki, K.S.; Moattari, M.; Shafiei, A.; Amirjan, M. On the failure behavior of fifth stage gas turbine blade. *Eng. Fail. Anal.* **2020**, *116*, 104766. [CrossRef]

15. Klochikhin, V.; Naumyk, V. Improvement of technological processes obtaining a heat-resistant nickel alloys for turbine blades using foundry return. *Mater. Sci. Technol.* **2019**, *1*, 1454. [CrossRef]

16. Rayapati, S. Gas turbine blade failure scenario due to thermal loads in case of Nickel based super alloys. *Mater. Today Proc.* **2021**, *46*, 8119–8126. [CrossRef]

17. Kuznetsov, P.; Lesnikov, V.P.; Konakova, I.P.; Popov, N.A.; Kvasnitskaya, Y.G. Structural and phase transformations in single-crystal rhenium- and ruthenium-alloyed nickel alloy under testing for long-term strength. *Met. Sci. Heat Treat.* **2015**, *57*, 503–506. [CrossRef]

18. Wu, X.; Makineni, S.K.; Liebscher, C.H.; Dehm, G.; Mianroodi, J.R. Unveiling the Re effect in Ni-based single crystal superalloys. *Nat. Commun.* **2020**, *11*, 389. [CrossRef] [PubMed]

19. Hlotka, A.A.; Haiduk, S.V. Prediction of the thermodynamic processes of phase separation in single-crystal refractory alloys based on nickel. *Mater. Sci.* **2020**, *54*, 878–883. [CrossRef]

20. Rajabinezhad, M.; Bahrami, A.; Mousavinia, M.; Seyedi, S.J.; Taheri, P. Corrosion-fatigue failure of gas-turbine blades in an oil and gas production plant. *Materials* **2020**, *13*, 900. [CrossRef]

21. Kvasnytska, Y.H.; Ivaskevych, L.M.; Balytskyi, O.I.; Maksyuta, I.I.; Myalnitsa, H.P. High-temperature salt corrosion of a heat-resistant nickel alloy. *Mater. Sci.* **2020**, *56*, 432. [CrossRef]

22. Reising, R.F. High temperature corrosion of nickel by sodium sulffat. *Corrosion* **1977**, *33*, 84–91. [CrossRef]

23. Sims, C.T.; Stoloff, N.S.; Hagel, W.C. *Superalloys II: High-Temperature Materials for Aerospace and Industrial Power*; John Wiley & Sons: New York, NY, USA, 1987; 640p, Available online: https://www.wiley.com/en-us/Superalloys+II%3A+High+Temperature+Materials+for+Aerospace+and+Industrial+Power-p-9780471011477 (accessed on 27 November 2022).

24. Makineni, S.K.; Lenz, M.; Neumeier, S.; Spiecker, E.; Raabe, D.; Gault, B. Elemental segregation to antiphase boundaries in a crept CoNi-based single crystal superalloy. *Scr. Mater.* **2018**, *157*, 62–66. [CrossRef]

25. Balitskii, O.I.; Kvasnytska, Y.H.; Ivaskevych, L.M.; Mialnitsa, H.P.; Kvasnytska, K.H. Fatigue fracture of the blades of gas turbine engine made of a new refractory nickel alloy. *Mater. Sci.* **2022**, *57*, 475–483. [CrossRef]

26. Kvasnytska, Y.H.; Ivaskevich, L.M.; Balitskii, A.I.; Kvasnytska, K.H.; Mialnitsa, H.P. Structural and mechanical properties of the nickel alloy of gas-turbine engine blades. *Mater. Sci.* **2022**, *57*, 688–694. [CrossRef]

27. Balyts'kyi, O.I.; Chmiel, J.; Krause, P.; Niekrasz, J.; Maciag, M. Role of hydrogen in the cavitation fracture of 45 steel in lubricating media. *Mater. Sci.* **2009**, *45*, 651–654. [CrossRef]

28. Balyts'kyi, O.I.; Ivas'kevych, L.M.; Mochul's'kyi, V.M.; Holiyan, O.M. Influence of hydrogen on the crack resistance of 10Kh15N27T3V2MR steel. *Mater. Sci.* **2009**, *45*, 258–267. [CrossRef]

29. Balyts'kyi, A.I.; Kvasnyts'ka, Y.H.; Ivas'kevich, L.M.; Myal'nitsa, H.P. Corrosion and Hydrogen-Resistance of Heat-Resistant Blade Nickel-Cobalt Alloys. *Mater. Sci.* **2018**, *54*, 230–239. [CrossRef]

30. Zhang, Z.; Obasi, G.; Morana, R.; Preuss, M. In-Situ observation of hydrogen induced crack initiation in a nickel-based superalloy. *Scr. Mater.* **2017**, *140*, 40–44. [CrossRef]

31. Šmíd, M.; Horník, V.; Kunz, L.; Hrbáček, K.; Hutař, P. High cycle fatigue data transferability of MAR-M 247 superalloy from separately cast specimens to real gas turbine blade. *Metals* **2020**, *10*, 1460. [CrossRef]

32. Mytsyk, B.G.; Ivanytskyi, Y.L.; Balitskii, A.I.; Kost', Y.P.; Sakharuk, O.M. Study of hydrogen influence on 1020 steel by low deformation method. *Mater. Lett.* **2016**, *184*, 328–331. [CrossRef]

33. Zhoua, P.J.; Yub, J.J.; Sunb, X.F.; Guanb, H.R.; Hec, X.M.; Hub, Z.Q. Influence of Y on stress rupture property of a Ni-based superalloy. *Mat. Sci. Eng. A* **2012**, *551*, 236–240. [CrossRef]

34. Amouyal, Y.; Seidman, D.N. The role of hafnium in the formation of misoriented defects in Ni-based superalloys: An atomprobe tomographic study. *Acta Mater.* **2011**, *59*, 3321–3333. [CrossRef]

35. Chen, S.; Zhao, M.; Rong, L. Effect of grain size on the hydrogen embrittlement sensitivity of a precipitation strengthened Fe-Ni based alloy. *Mat. Sci. Eng. A* **2014**, *594*, 98–102. [CrossRef]

36. Tkachov, V.I.; Levina, I.M.; Ivas'kevych, L.M. Distinctive features of hydrogen hydrogen degradation of heat-resistance alloys based on nickel. *Mater. Sci.* **1997**, *33*, 524–531. [CrossRef]

37. Balitskii, A. Hydrogen assisted crack initiation and propagation in nickel-cobalt heat resistant superalloys. *Procedia Struct. Integr.* **2019**, *16*, 134–140. [CrossRef]

38. Lee, A. Hydrogen embrittlement of nickel, cobalt and iron-based superalloys. In *The Problem, Its Characterization and Effects on Particular Alloy Classes. Gaseous Hydrogen Embrittlement of Materials in Energy Technologies, Volume 1*; Gangloff, R.P., Somerday, B.P., Eds.; Woodhead Publishing Limited.: Oxford, UK; Cambridge, UK; Philadelphia, PA, USA; New Delhi, India, 2012; pp. 624–667. Available online: https://www.sciencedirect.com/science/article/pii/B978184569677150017X?via%3Dihub (accessed on 27 November 2022). [CrossRef]

39. Balitskii, A.; Ivaskevich, L.; Mochulskyi, V.; Eliasz, J.; Skolozdra, O. Influence of high pressure and high temperature hydrogen on fracture toughness of Ni-containing steels and alloys. *Arch. Mech. Eng.* **2014**, *61*, 129–138. [CrossRef]

40. Taji, I.; Hajilou, T.; Karimi, S.; Schott, F.; Plesiutschnig, E.; Barnoush, A.; Johnsen, R. Role of grain boundaries in hydrogen embrittlement of alloy 725: Single and bi-crystal microcantilever bending study. *Int. J. Hydrog. Energy* **2022**, *47*, 12771–12781. [CrossRef]

41. Taji, I.; Hajilou, T.; Ebner, A.S.; Scheiber, D.; Karimi, S.; Plesiutschnig, E.; Ecker, W.; Barnoush, A.; Maier-Kiener, V.; Johnsen, R.; et al. Hydrogen assisted intergranular cracking of alloy 725: The effect of boron and copper alloying. *Corros. Sci.* **2022**, *203*, 110331. [CrossRef]

42. Balitskii, A.I.; Ivaskevich, L.M. Hydrogen effect on cumulation of failure, mechanical properties, and fracture toughness of Ni-Cr alloys. *Adv. Mat. Sci. Eng.* **2019**, *2019*, 3680253. [CrossRef]

43. *ASTM G129-2000(R2013)*; Standard Practice for Slow Strain Rate Testing to Evaluate the Susceptibility of Metallic Materials to Environmentally Assisted Cracking. American Society for Testing Material: West Conshohocken, PA, USA, 2013; p. 129. Available online: https://webstore.ansi.org/standards/astm/astmg129002013 (accessed on 27 November 2022).

44. Djukic, M.; Curtin, W.A.; Zhang, Z.; Sedmak, A. Recent advances on hydrogen embrittlement understanding and future research framework. *Eng. Fract. Mech.* **2021**, *241*, 107439. [CrossRef]

45. Ogawa, Y.; Noguchi, K.; Takakuwa, O. Criteria for hydrogen-assisted crack initiation in Ni-based superalloy 718. *Acta Mater.* **2022**, *229*, 117789. [CrossRef]

46. Harris, Z.D.; Bhattacharyya, J.J.; Ronevich, J.A.; Agnew, S.R.; Burns, J.T. The combined effects of hydrogen and aging condition on the deformation and fracture behavior of a precipitation-hardened nickel-base superalloy. *Acta Mater.* **2020**, *186*, 616–630. [CrossRef]

47. Balyts'kyi, O.I.; Ivas'kevych, L.M.; Eliasz, J.J. Static Crack Resistance of Heat-Resistant KhN43MBTYu Nickel-Chromium Alloy in Gaseous Hydrogen. *Strength Mater.* **2020**, *52*, 386–397. [CrossRef]

48. Balitskii, A.I.; Ivaskevich, L.M.; Balitskii, O.A. Rotor steels crack resistance and fracture behavior for hydrogen targeted materials ever-widening database. *Eng. Fract. Mech.* **2022**, *260*, 108168. [CrossRef]

49. Panasyuk, V.V.; Dmytrakh, I.M.; Toth, L.; Bilyi, O.L.; Syrotyuk, A.M. A method for the assessment of the serviceability and fracture hazard for structural elements with cracklike defects. *Mater. Sci.* **2014**, *49*, 565–576. [CrossRef]

50. Balitskii, A.I.; Dmytryk, V.V.; Ivaskevich, L.M.; Balitskii, O.A.; Glushko, A.V.; Medovar, L.B.; Abramek, K.F.; Stovpchenko, G.P.; Eliasz, J.J.; Krolikowski, M.A. Improvement of the Mechanical Characteristics, Hydrogen Crack Resistance and Durability of Turbine Rotor Steels Welded Joints. *Energies* **2022**, *15*, 6006. [CrossRef]

51. Aksimentyeva, O.I.; Demchenko, P.Y.; Savchyn, V.P.; Balitskii, O.A. The chemical exfoliation phenomena in layered GaSe-polyaniline composite. *Nanoscale Res. Lett.* **2013**, *8*, 29. [CrossRef] [PubMed]

52. Rozumek, D.; Macha, E. Elastic-plastic fatigue crack growth in 18G2A steel under proportional bending with torsion loading. *Fatigue Fract. Eng. Mater. Struct.* **2006**, *29*, 135–145. [CrossRef]

53. Moustabchir, H.; Azari, Z.; Hairi, S.; Dmytrakh, I. Experimental and computed stress distribution ahead of notch in pressure vessel: Application of T-stress conception. *Comput. Mater. Sci.* **2012**, *58*, 59–66. [CrossRef]

54. Karpenko, G.V.; Litvin, A.K.; Tkachev, V.I.; Soshko, A.I. Mechanism of hydrogen embrittlement. *Sov. Mater. Sci.* **1975**, *9*, 367–371. [CrossRef]

55. Rozumek, D.; Marciniak, Z. Fatigue properties of notched specimens made of FeP04 Steel. *Mater. Sci.* **2012**, *47*, 462–469. [CrossRef]

56. Kozak, L.Y. Discrete models of plastic deformation of solids under the action of high hydrostatic pressure. *Mater. Sci.* **2016**, *52*, 108–112. [CrossRef]

57. Balitskii, O.A.; Savchyn, V.P.; Savchyn, P.V. Thermal oxidation of indium and gallium sulphides. *Phys. B Condens. Matter* **2005**, *355*, 365–369. [CrossRef]

58. Romaniv, O.N.; Nikiforchin, G.N.; Kozak, L.Y. Structural sensitivity of the cyclic crack resistance of rotor steel in gaseous hydrogen. *Sov. Mater. Sci.* **1984**, *20*, 424–429. [CrossRef]

59. Romaniv, O.N.; Nikiforchin, G.N.; Kozak, L.Y. Cyclic rack resistance of constructional steel in gaseous hydrogen. *Sov. Mater. Sci.* **1987**, *23*, 439–450. [CrossRef]

60. Syrotyuk, A.M.; Dmytrakh, I.M. Methods for the evaluation of fracture and strength of pipeline steels and structures under the action of working media. Part II: Influence of hydrogen-containing media. *Mater. Sci.* **2015**, *50*, 475–487. [CrossRef]

61. Dmytrakh, I.M.; Leshchak, R.L.; Syrotyuk, A.M.; Barna, R.A. Effect of hydrogen concentration on fatigue crack growth behaviour in pipeline steel. *Int. J. Hydrog. Energy* **2017**, *42*, 6401–6408. [CrossRef]

62. Zima, Y.V.; Kozak, L.Y. Fractographic aspects of the cyclic crack resistance of 35KhN3MFA steel in vacuum, air, and hydrogen. *Mater. Sci.* **1986**, *22*, 268–275. [CrossRef]

63. Bihun, R.I.; Stasyuk, Z.V.; Balitskii, O.A. Crossover from quantum to classical electron transport in ultrathin metal films. *Phys. B Condens. Matter* **2016**, *487*, 73–77. [CrossRef]

64. Capelle, J.; Dmytrakh, I.; Gilgert, J.; Jodin, P.; Pluvinage, G. A comparison of experimental results and computations for ctacked tubes subjected to internal pressure. *Mat. Technol.* **2006**, *40*, 233–237.

65. Benghalia, M.A.; Faces, C.; Khadrauui, A.; Meliani, M.H.; Obot, I.B.; Sorrour, A.; Dmytrakh, M.; Azari, Z. Performance evaluation of a natural and synthetic compound as corrosion inhibitors of API 5l X52 steel in hydrochloric acid media. *Moroc. J. Chem.* **2018**, *6*, 51–61. [CrossRef]

66. Akid, R.; Dmytrakh, I.M.; Gonzalez-Sanchez, J. Fatigue damage accumulation: The role of corrosion on the early stages of crack development. *Corros. Eng. Sci. Technol.* **2006**, *41*, 328–335. [CrossRef]

67. Olmi, G.; Freddi, A. Low cycle fatigue behavior and anisotropy of two steels for turbogenerator coil retaining ring and rotors. In Proceedings of the 9th Youth Symposium on Experimental Solid Mechanics, Trieste, Italy, 7–10 July 2010; pp. 188–192, ISBN 978-88-95940-30-4. Available online: https://www.semanticscholar.org/paper/Low-cycle-fatigue-behaviour-and-anisotropy-of-two-Olmi-Freddi/6a7b4c86f579967fa26aa7062db32c01119a2743 (accessed on 27 November 2022).

68. Olmi, G. An efficient method for the determination of the probability of failure on the basis of LCF data: Application to turbogenerator design. *Struct. Durab. Health Monit.* **2012**, *8*, 61–89.

69. Krasovskii, A.Y.; Vainshtok, V.A. Use of fracture mechanics to evaluate the bearing capacity and remaining life of rotors in turbomachinery. *Strength Mater.* **1982**, *14*, 997–1005. [CrossRef]

70. Eckardt, D.; Rufli, P. Advanced gas turbine technology: ABB/BCC historical first. *Trans. ASME* **2002**, *124*, 542–549. [CrossRef]

71. Balitskii, O.; Borowiak-Palen, E.; Konicki, W. Synthesis and characterization of colloidal gallium selenide nanowires. *Cryst. Res. Technol.* **2011**, *46*, 417–420. [CrossRef]

72. Dmytrakh, I.M.; Akid, R.; Miller, K.J. Electrochemistry of deformed smooth surfaces and short corrosion fatigue crack growth behaviour. *Br. Corros. J.* **1997**, *32*, 138–144. [CrossRef]

73. Syrotyuk, A.M.; Dmytrakh, I.M. Methods for the evaluation of fracture and strength of pipeline steels and structures under the action of working media. Part I. Influence of the corrosion factor. *Mater. Sci* **2014**, *50*, 324–339. [CrossRef]

74. Charpagne, M.A.; Polonsky, A.T.; Echlin, M.P.; Jacomet, S.; De Jaeger, J.; De Graef, N.; Bozzolo, T.; Pollock, M. Growth accidents induced by primary γ' precipitates in a polycrystalline nickel-based superalloy. *Scr. Mater.* **2020**, *186*, 109–113. [CrossRef]

75. Balitska, V.; Shpotyuk, Y.; Filipecki, J.; Shpotyuk, O.; Iovu, M. Post-irradiation relaxation in vitreous arsenic/antimony trisulphides. *J. Non-Cryst. Solids* **2011**, *357*, 487–489. [CrossRef]

76. Ogawa, Y.; Hosoi, H.; Tsuzaki, K.; Redarce, T.; Takakuwa, O.; Matsunaga, H. Hydrogen, as an alloying element, enables a greater strength-ductility balance in an Fe-Cr-Ni-based, stable austenitic stainless steel. *Acta Mater.* **2020**, *199*, 181–192. [CrossRef]

77. Michler, T.; Naumann, J.; Balogh, M.P. Hydrogen environment embrittlement of solution treated Fe–Cr–Ni super alloys. *Mat. Sci. Eng. A.* **2014**, *607*, 71–80. [CrossRef]

78. Zhang, Z.; Obasis, G.; Morana, R.; Preuss, M. Hydrogen assisted crack initiation and propagation in a nickel-based superalloy. *Acta Mater.* **2016**, *113*, 272–283. [CrossRef]

79. Guédou, J.-Y.; Augustins-Lecallier, I.; Nazé, L.; Caron, P.; Locq, D. Development of a new fatigue and creep resistant PM nickel-base superalloy for disk applications. *Superalloys* **2008**, *1*, 21–30. [CrossRef]

80. Furrer, D.; Fecht, H. Ni-based superalloys for turbine discs. *JOM* **1999**, *51*, 14–17. [CrossRef]

81. Drexler, A.; He, S.; Pippan, R.L.; Romaner, V.; Razumovskiy, I.; Ecker, W. Hydrogen segregation near a crack tip in nickel. *Scr. Mater.* **2021**, *194*, 113697. [CrossRef]

82. Tarzimoghadam, Z.; Rohwerder, M.; Merzlikin, S.V.; Bashir, A.; Yedra, L.; Eswara, S.; Ponge, D.; Raabe, D. Multi-scale and spatially resolved hydrogen mapping in a Ni–Nb model alloy reveals the role of the δ phase in hydrogen embrittlement of alloy 718. *Acta Mater.* **2016**, *109*, 69–81. [CrossRef]

83. Ma, D.; Blazej Grabowski, B.; Körmann, F.; Neugebauer, J.; Raabe, D. Ab initio thermodynamics of the CoCrFeMnNi high entropy alloy: Importance of entropy contributions beyond the configurational one. *Acta Mater.* **2015**, *100*, 90–97. [CrossRef]

84. Shpotyuk, O.I.; Balitska, V.O.; Vakiv, M.M.; Shpotyuk, L.I. Sensors of high-energy radiation based on amorphous chalcogenides. *Sens. Actuators A Phys.* **1998**, *68*, 356–358. [CrossRef]

85. Tarzimoghadam, Z.; Ponge, D.; Klöwer, J.; Raabe, D. Hydrogen-assisted failure in Ni-based superalloy 718 studied under in situ hydrogen charging: The role of localized deformation in crack propagation. *Acta Mater.* **2017**, *128*, 365–374. [CrossRef]

86. Povstugar, I.; Choi, P.-P.; Neumeier, S.; Bauer, A.; Christopher, H.; Göken, Z.M.; Raabe, D. Elemental partitioning and mechanical properties of Ti- and Ta-containing Co–Al–W-base superalloys studied by atom probe tomography and nanoindentation. *Acta Mater.* **2014**, *78*, 78–85. [CrossRef]

87. Michler, T. Influence of gaseous hydrogen on the tensile properties of Fe–36Ni INVAR alloy. *Int. J. Hydrogen Energy* **2014**, *39*, 11807–11809. [CrossRef]

88. Ma, D.; Yao, M.; Pradeep, V.; Tasan, C.C.; Springer, H.; Raabe, D. Phase stability of non-equiatomic CoCrFeMnNi high entropy alloys. *Acta Mater.* **2015**, *98*, 288–296. [CrossRef]

89. Chauvet, E.; Kontis, P.; Jägle, E.A.; Gault, B.; Raabe, D.; Tassin, C.; Blandin, J.-J.; Dendievel, R.; Vayre, B.; Abed, S.; et al. Hot cracking mechanism affecting a non-weldable Ni-based superalloy produced by selective electron beam melting. *Acta Mater.* **2018**, *142*, 82–94. [CrossRef]

90. Tytko, D.; Choi, P.-P.; Klöwer, J.; Kostka, A.; Inden, G.; Raabe, D. Microstructural evolution of a Ni-based superalloy (617B) at 700°C studied by electron microscopy and atom probe tomography. *Acta Mater.* **2012**, *60*, 1731–1740. [CrossRef]

91. Matuszewski, K.; Rettig, R.; Matysiak, H.; Peng, Z.; Povstugar, I.; Choi, P.; Müller, J.; Raabe, D.; Spiecker, E.; Kurzydłowski, K.J.; et al. Effect of ruthenium on the precipitation of topologically close packed phases in Ni-based superalloys of 3rd and 4th generation. *Acta Mater.* **2015**, *95*, 274–283. [CrossRef]

92. Kontis, P.; Chauvet, E.; Peng, Z.; He, J.; Kwiatkowski, A.; Silva, D.; Raabe, D.; Tassin, C.; Blandin, J.J.; Abed, S.; et al. Atomic-scale grain boundary engineering to overcome hot-cracking in additively-manufactured superalloys. *Acta Mater.* **2019**, *177*, 209–221. [CrossRef]

93. Haghighat, S.M.H.; Eggeler, G.; Raabe, D. Effect of climb on dislocation mechanisms and creep rates in γ'-strengthened Ni base superalloy single crystals: A discrete dislocation dynamics study. *Acta Mater.* **2013**, *61*, 3709–3723. [CrossRef]

94. Djukic, M.B.; Bakic, G.M.; Zeravcic, V.S.; Sedmak, A.; Rajicic, B. The synergistic action and interplay of hydrogen embrittlement mechanisms in steels and iron: Localized plasticity and decohesion. *Eng. Fract. Mech.* **2019**, *216*, 106528. [CrossRef]

95. Wasim, M.; Djukic, M.; Ngo, T.D. Influence of hydrogen-enhanced plasticity and decohesion mechanisms of hydrogen embrittlement on the fracture resistance of steel. *Eng. Fail. Anal.* **2021**, *123*, 105312. [CrossRef]

96. Glotka, O.A. Distribution of alloying elements in carbides of refractory nickel alloys under the conditions of equiaxial crystallization. *Mater. Sci.* **2021**, *56*, 714–721. [CrossRef]

97. Wasim, M.; Djukic, M. Hydrogen embrittlement of low carbon structural steel at macro-, micro- and nano-levels. *Int. J. Hydrogen Energy* **2020**, *45*, 2145–2156. [CrossRef]

98. Prakash, A.; Guénolé, J.; Wang, J.; Müller, J.; Spiecker, E.; Mills, M.J.; Povstugar, I.; Choi, P.; Raabe, D.; Bitzek, E. Atom probe informed simulations of dislocation–precipitate interactions reveal the importance of local interface curvature. *Acta Mater.* **2015**, *92*, 33–45. [CrossRef]

99. Ram, F.; Li, Z.; Zaefferer, S.; Masood, S.; Haghighat, H.; Zhu, Z.; Raabe, D.; Roger, C.; Reed, R.C. On the origin of creep dislocations in a Ni-base, single-crystal superalloy: An ECCI, EBSD, and dislocation dynamics-based study. *Acta Mater.* **2016**, *109*, 151–161. [CrossRef]

100. Neeraj, T.; Srinivasan, R.; Li, J. Hydrogen embrittlement of ferritic steels: Observations on deformation microstructure, nanoscale dimples and failure by nanovoiding. *Acta Mater.* **2012**, *60*, 5160–5171. [CrossRef]

101. Teus, S.M.; Mazanko, V.F.; Plive, J.-M.; Gavrilijuk, V.G. Grain boundary migration of substitutional and interstitial atoms in α-iron. *Acta Mater.* **2012**, *69*, 105–113. [CrossRef]

102. Van Sluytman, J.S.; Pollock, T.M. Optimal precipitate shapes in nickel-base γ–γ' alloys. *Acta Mater.* **2012**, *60*, 1771–1783. [CrossRef]

103. Bezold, A.; Volz, N.; Lenz, M.; Karpstein, N.; Zenk, C.H.; Spiecker, E.; Göken, M.; Neumeier, S. Quantification of the temperature-dependent evolution of defect structures in a CoNi-base superalloy. *Acta Mater.* **2022**, *227*, 117702. [CrossRef]

104. Zhang, X.; Sergiy, V.; Divinski, S.V.; Blazej Grabowski, B. Ab initio prediction of vacancy energetics in HCP Al-Hf-Sc-Ti-Zr high entropy alloys and the subsystems. *Acta Mater.* **2022**, *227*, 117677. [CrossRef]

105. Balitska, V.; Filipecki, J.; Shpotyuk, O.; Swiatek, J.; Vakiv, M. Dynamic radiation-induced effects in chalcogenide vitreous compounds. *J. Non-Cryst. Solids* **2001**, *287*, 216–221. [CrossRef]

106. Glotka, O.A.; Gayduk, S.V.; Olshanetskiy, V.Y. The distribution of alloying elements in secondary carbides of heat-resistant nickel alloys. *Metalozn. Obrobka Met.* **2020**, *26*, 25–36. [CrossRef]

107. Glotka, A.A.; Haiduk, S.V.; Ol'shanetskii, V.Y. Modeling thermophysical characteristics of nickel-based superalloys. *J. Eng. Phys. Thermophys.* **2021**, *94*, 1363–1368. [CrossRef]

108. Rezende, C.; Araujo, L.S.; Gabriel, S.B.; dos Santos, D.S.; de Almeida, L.H. Hydrogen embrittlement in nickel-based superalloy 718: Relationship between γ' + γ'' precipitation and the fracture mode. *Int. J. Hydrogen Energy* **2015**, *40*, 17075–17083. [CrossRef]

109. New Energy and Industrial Technology Development Organization. *International Clean Energy Network Using Hydrogen Conversion (WE-NET). 1993 Annual Summary Report on Results (NEDO-WE-NET-93)*; New Energy and Industrial Technology Development Organization: Kawasaki, Japan, 1994; 84p. Available online: https://www.osti.gov/etdeweb/servlets/purl/20316293 (accessed on 27 November 2022).

110. Kozakiewicz, A.; Jóźwiak, S.; Jóźwiak, P.; Kachel, S. Material origins of the accelerated operational wear of RD-33 engine blades. *Materials* **2021**, *14*, 336. [CrossRef] [PubMed]

111. Liu, B.; Raabe, D.; Roters, F.; Arsenlis, A. Interfacial dislocation motion and interactions in single-crystal superalloys. *Acta Mater.* **2014**, *79*, 216–233. [CrossRef]

112. Ryś, J. *Quantitative Metallography*; AGH: Krakow, Poland, 1983; 280p.

113. Gao, Z.; Tan, J.; Guo, W.; Zhang, C.; Zhang, W. Characterization of the microstructure evolution of Ni-based superalloy at liquidus temperature by electromagnetic field. *Metals* **2018**, *8*, 748. [CrossRef]

114. Pearson, K. *The Grammar of Science*; Dover Phoenix Editions; Cosimo Classics: New York, NY, USA, 2004; 416p.

115. Wahl, J.B.; Harris, K. CMSX-4 plus single alloy development, characterization and application development. In *Superalloys 2016: Proceedings of the 13th International Symposium on Superalloys, TMS (the Minerals, Metals & Materials Society), Seven Springs, PA, USA, 11–15 September 2016*; Wiley: Hoboken, NJ, USA, 2016; pp. 25–33.